12th International Symposium on Turbulence and Shear Flow Phenomena (TSFP12)
Osaka, Japan (Online), July 19-22, 2022

TOWARDS A GENERALIZABLE DATA-DRIVEN APPROACH TO PREDICT SEPARATION-INDUCED TRANSITION

Vishal Srivastava
Department of Aerospace Engineering
University of Michigan
Ann Arbor, MI 48105
vsriv@umich.edu

Karthik Duraisamy
Department of Aerospace Engineering
University of Michigan
Ann Arbor, MI 48105
kdur@umich.edu

ABSTRACT

This work introduces a hierarchical data-driven model augmentation technique to alleviate structural inadequacies in a transition model. This technique is demonstrated by introducing two different model augmentations, β_1 and β_2 within Wilcox's 1988 k-ω turbulence model. These functions are consecutively inferred in a model-consistent fashion as functions of local flow quantities to improve predictions for bypass transition caused by freestream disturbances and flow separation, respectively. The key step described in the process is designing a physics-informed blending function to isolate the effects of the β_2 only to cases involving flow separation. β_1 is inferred from only two flat plate cases from the ERCOFTAC dataset, whereas LES data for only one compressor cascade case is used to infer β_2. While both, β_1 and β_2, consistently improve predictive accuracy across all unseen test cases, it is observed that transition is predicted significantly upstream for cases involving transition of attached flow under adverse pressure gradients, and some cases involving flow separation.

INTRODUCTION

While Reynolds-Averaged Navier-Stokes (RANS) simulations have been the industry workhorse for applications involving design and optimization of flow paths, turbulence closures used in RANS models consist of model-form inadequacies that can result in significant prediction errors for cases involving complex geometries or unseen physical conditions. Over the past decade, the emergence of machine learning as a scientific tool has led to the development of several data-driven frameworks that can extract corrections to reduced-fidelity models from high-fidelity data. These include the Field Inversion and Machine Learning (FIML) framework by Parish & Duraisamy (2016), Integrated Inference and Machine Learning (IIML) by Holland *et al.* (2019), Sparse Regression of Turbulence Stress Anisotropy (SpaRTA) by Schmelzer *et al.* (2020), Deep learning PDE Model (DPM) by Sirignano *et al.* (2020), Data Assimilation and Machine Learning by Volpiani *et al.* (2021), End-to-end Differentiable Learning by Ströfer & Xiao (2021), and EVolutionary algorithm for the development of Expressions (EVE) by Waschkowski *et al.* (2022) among others. It should be noted, however, that model augmentations extracted using several of these frameworks struggle to improve predictive accuracy across a wide range of geometries and physical conditions.

Srivastava & Duraisamy (2021) presented Learning and Inference assisted by Feature-space Engineering (LIFE) framework which is based on the IIML framework by Holland *et al.* (2019) and provides expert modelers with guiding principles, tools and techniques to extract generalizable, robust and model-consistent augmentations from limited data. This work presents a hierarchical model augmentation strategy via the LIFE framework that involves consecutive introduction and inference of two augmentation functions, β_1 and β_2, into a baseline turbulence model to enable prediction of bypass transition caused by freestream disturbances and flow separation, respectively. The robustness offered by the LIFE framework (by reverting to baseline model behavior within feature-space regions where no training data is available) makes it easier to infer hierarchical augmentations. Designing an appropriate blending function is key to extend the applicability of hierarchically augmented models to a wide range of geometries and operating conditions. A blending function, σ, is designed in this work to isolate the effects of the hierarchical augmentation to cases involving flow separation.

METHODOLOGY

The LIFE framework is explained as follows. Assume that a baseline model is given as $\mathscr{R}(u;\xi) = 0$ where u and ξ represent the model states and the inputs to the model (mesh, boundary conditions, etc.), respectively. An augmentation function $\beta(\eta(u;\xi);w)$ is then carefully introduced within the model such that it can modify model behavior for physical conditions affected by the inadequacy in consideration and has a minimal influence on other physical conditions. The augmented model can then be written as $\mathscr{R}(u,\beta(\eta(u;\xi));w)) = 0$. Here η refers to features which are local geometrically invariant quantities derived from model states. The additional dependence of η on ξ is to account for features be-

ing functions of quantities like wall distance or gradients of model states. The augmentation function β is characterized by function parameters w. The LIFE framework offers several guiding principles for feature design, the major ones among which include choice of features relevant to the inadequacy in consideration, physics-based (instead of statistics-based) non-dimensionalization, a bounded functional form for features, and ensuring that physical conditions that require different augmentation values are manifested in different regions within the feature-space. In addition to these guidelines, LIFE also introduces localized learning techniques to ensure that the augmentation behavior remains unchanged in the feature-space regions that do not contain data. This offers robustness and ensures that the augmented model falls back to its baseline behavior for unseen physical conditions. To infer the optimal values of these parameters from available data, the inverse problem shown in Eqn. 1 is solved.

$$w^* = \arg\min_w \sum_{k=1}^{N} [\mathscr{C}^k(y^k_{\text{data}}, y^k_{\text{pred}}(u^k;\xi^k)) + \lambda^k \mathscr{T}^k(\beta(\eta(u^k;\xi^k);w))] \tag{1}$$

Here, k is the index assigned to individual training datasets, $\mathscr{C}$ refers to the cost function defining the discrepancy between sparsely available data and corresponding predictions for quantities y, and $\mathscr{T}$ refers to a regularization function. Once the minimization problem is solved, the optimal weights w^* can be used within the augmented solver for predictions as $\mathscr{R}(u,\beta(\eta(u;\xi));w^*)) = 0$. Note that this work does not use any explicit regularization as there is ample implicit regularization as a consequence of inference from multiple cases, the augmentation function being a function of specified features and even the underlying functional form of the augmentation being constrained in the feature-space.

Augmenting Wilcox's 1988 k-ω model

A bare-bones intermittency transport equation, inspired from the model by Durbin (2012), was added to Wilcox's 1988 k-ω model (Wilcox (1988)) and augmented as shown in Eqn. 2.

$$\begin{aligned}
\frac{D(\rho k)}{Dt} &= \nabla\cdot((\mu+\sigma_k\mu_t)\nabla k) + \gamma P_k - C_\mu \rho k\omega \\
\frac{D(\rho \omega)}{Dt} &= \nabla\cdot((\mu+\sigma_\omega\mu_t)\nabla \omega) + C_{\omega 1}\frac{\omega}{k}P_k - C_{\omega 2}\rho\omega^2 \\
\frac{D(\rho \gamma)}{Dt} &= \nabla\cdot\left((\sigma_{\gamma,\ell}\mu+\sigma_{\gamma,t}\mu_t)\nabla k\right) + \rho\Omega(\beta_1\beta_2^\sigma - \gamma)\sqrt{\gamma}
\end{aligned} \tag{2}$$

Here, the production of turbulent kinetic energy P_k is given as follows.

$$P_k = \mu_t\Omega^2 - \frac{2}{3}\rho k\frac{\partial u_i}{\partial x_i}$$

The main differences compared to Durbin's model are that the $\gamma_{\max}$ term is replaced by $\beta_1\beta_2^\sigma$, and that the function F_γ is absent from the source term. β_1 is inferred using data from only two flat plate cases to enable predictions for bypass transition due to freestream disturbances. β_2 is inferred from only a single compressor cascade case (after β_1 is inferred) to enable predictions of separation-induced bypass transition. The blending function σ can vary between zero and unity and acts as an automatic switch to activate/deactivate the β_2 augmentation depending on whether the flow exhibits flow separation. The baseline value for β_1, β_2 and σ is unity which makes $\gamma = 1$ everywhere in the physical domain, hence ensuring baseline k-ω model predictions. It should be noted here that two augmentation functions are needed because a single augmentation function was unable to establish a functional relationship consistent with bypass transition originating due to both, freestream disturbances as well as flow separation. Given how the augmentation term is introduced in the model, the spatial field for intermittency (γ) closely resembles the $\beta_1\beta_2^\sigma$ field. A transport equation is used, instead of directly multiplying the source term in the k-equation with $\beta_1\beta_2^\sigma$, because it provides a smoother field for the solver to work with, hence preserving stability and also because it brings in the effects of flow history within the intermittency.

Feature Design

The features used in this work are identical to those proposed by Srivastava & Duraisamy (2021). Both, β_1 and β_2 are functions of the same three features. These features are briefly described as follows.

$$\eta_1 = \min\left(\frac{d_w^2\Omega}{2.188U_\infty}\sqrt{\frac{9\omega_\infty}{7\nu}}, 3\right) \tag{3}$$

The first feature is the ratio of the vorticity Reynolds number $Re_\Omega = d_w^2\Omega/(2.188\nu)$ (see Durbin (2012)) and $Re_{\theta,tr}$, where θ_{tr} is the correlation for transition momentum thickness given by Praisner & Clark (2004) as $\theta_{tr} = \sqrt{7\nu/9\omega_\infty}$. All freestream quantities are extracted from a user-specified distance away from the wall. A conservative upper-bound of 3 is also explicitly applied.

$$\eta_2 = \frac{d_w\omega}{d_w\omega + \sqrt{k}} \tag{4}$$

$$\eta_3 = \frac{\nu}{\nu+\nu_t} \tag{5}$$

The second and third features distinguish the laminar boundary layer upstream of the transition location from near-wall regions in a turbulent boundary layer and turbulent flow regions, respectively. It should be noted here that it is in these laminar boundary layer regions where the augmentation values need to be significantly lower than their baseline value of unity.

Localized Learning

An interpolation-based C^0-continuous functional form was chosen to perform localized learning for this application. The feature-spaces corresponding to both, β_1 and β_2 were discretized into uniform grids. The augmentation values on the nodes of these grids act as function parameters, while the augmentation at any point in the feature-space is evaluated via multi-linear interpolation based on these nodal values (see Fig. 1). Note here that since the functional form is constrained to be C^0-continuous, sudden jumps in the augmentation values are not possible within the feature-space. On the other hand, the C^0-continuity provides for excellent convergence characteristics of the flow solver.

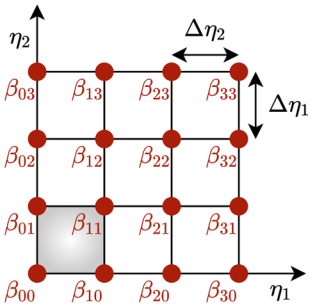

For a feature space location in the shaded region, the multilinear expression reads

$$\beta = \beta_{00} + (\beta_{10} - \beta_{00})\eta_1 + (\beta_{01} - \beta_{00})\eta_2 + \cdots (\beta_{11} + \beta_{00} - \beta_{10} - \beta_{01})\eta_1\eta_2$$

Figure 1. Schematic detailing C^0-continuous interpolation-based augmentation functions

Designing the Blending Function

To create a blending function σ that varies between zero and unity, one or more sigmoid functions can be applied to an appropriate quantity f_σ. Ge *et al.* (2014), used the function $\omega d_w(n_w \cdot \nabla)|S|/\sqrt{2}|S|^2$ to distinguish regions that exhibit flow separation. Here n_w is the wall-normal direction corresponding to the nearest point on the wall. This can be calculated by evaluating the gradient of the wall distance (d_w) and normalizing the result (to ensure that the magnitude is unity). Note that for body-fitted grids with low cell skewness, this approximation is fairly accurate close to the walls and that is exactly where the blending function is needed. $|S|$ denotes the magnitude of the strain rate tensor. Three changes were made to this function to formulate an appropriate f_σ that was found to effectively detect separated flow. The changes include the use of vorticity magnitude Ω instead of $|S|$, use of laminar length scale $\sqrt{\nu/\Omega}$ instead of d_w, and using a bounded functional form. The final functional form of f_σ is shown in Eqn. 6.

$$f_\sigma = \left(\frac{\sqrt{\nu}(n_w \cdot \nabla)\Omega}{\sqrt{\nu}|(n_w \cdot \nabla)\Omega| + \Omega^{1.5}}\right)\left(\frac{\omega}{\sqrt{2}\Omega + \omega}\right) \tag{6}$$

This function mainly targets the region within a separated flow where Ω increases with wall distance i.e., where f_σ is positive. However, it was seen that the σ needs to remain active for very small negative values of f_σ as well, to predict transition accurately for cases exhibiting separated boundary layers. This is probably because f_σ is positive in a very thin region and intermittency needs to be lowered within a slightly thicker region for k-production to sufficiently drop in order to predict transition at the correct location. The final functional form of σ is given in Eqn. 7.

$$\sigma = \frac{1}{1 + \exp(-(f_\sigma + 0.05)/0.003)} \tag{7}$$

RESULTS

This section describes the results obtained after inferring β_1 (β_2 assumed to be unity everywhere in the feature-space), inferring β_2 (β_1 frozen to its inferred form and $\sigma = 1$) and introducing the functional form for σ in a step-wise manner.

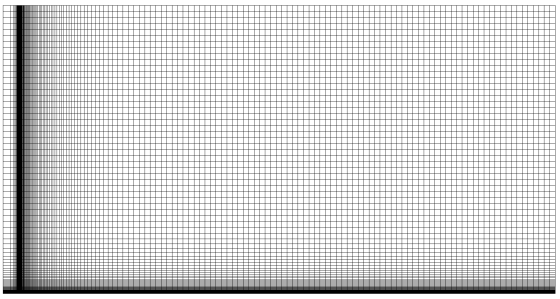

Figure 2. Mesh used for T3A and T3B cases

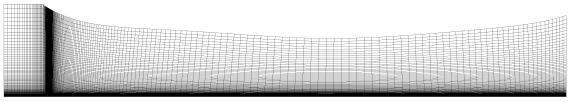

Figure 3. Mesh used for T3C1, T3C2, T3C3 and T3C5 cases

Table 1. Inflow conditions for the T3 test cases

Cases	Tu_{in}	$\nu_{t_{\text{in}}}$	L (in m)	$Re_{L,\text{in}}$
T3A	0.035	14.0	1.5	520000
T3C1	0.1	50.0	1.65	660000
T3B	0.065	100.0	1.5	940000
T3C2	0.037	12.0	1.65	550000
T3C3	0.034	8.0	1.65	418000
T3C5	0.043	17.0	1.65	946000

Inferring β_1

For this step, β_2 was constrained to unity for all regions in the feature space, which means all function parameters for β_2 were set to unity. Flat plate cases T3A and T3C1 from the ERCOFTAC dataset are used to train β_1 whereas other flat plate cases viz., T3B, T3C2, T3C3 and T3C5, were used to test the inferred augmentation. Meshes used for these cases can be seen in Figs. 2 and 3. The inflow conditions for all these cases are listed in Table 1.

Training Only cases T3A and T3C1 were used to infer function parameters β_1. Note here that transition occurs in a zero pressure gradient region for T3A and a favorable pressure gradient for T3C1. The training procedure is similar to that used by Srivastava & Duraisamy (2021). The cost functions for both these cases were chosen to be the sum squared discrepancy in the skin friction coefficients i.e., $\mathscr{C} = \|C_{f,\text{pred}} - C_{f,\text{data}}\|_2^2$. As stated previously, no regularization was used as ample implicit regularization is already present. The functional form corresponding to the interpolation-based C^0-continuous augmentation function was characterized by discretizing the feature-space into a grid with $45 \times 15 \times 15$ cells. Steepest gradient descent was used to solve the inference problem and the method of adjoints (along with automatic differentiation) was used to evaluate sensitivities. A step size of 0.1 was used. The intermittency was restricted within its physical bounds of 0 and 1 after every steepest gradient descent step. The corresponding predictions for both these cases

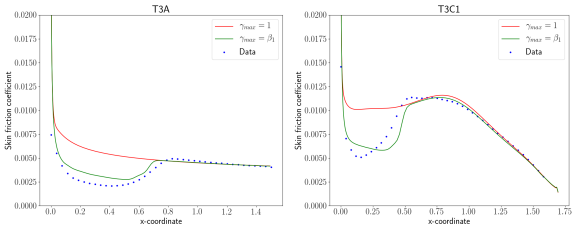

(a) T3A (b) T3C1

Figure 4. Skin friction predictions for T3C1. Blue dots - Data; Red curves - Predictions using baseline model; Green curves - Predictions with parameters inferred for β_1 only

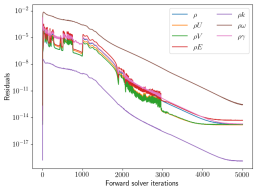

Figure 5. Residuals vs solver iterations

are shown in Fig. 4. The transition location is predicted well for both these cases while achieving better laminarization upstream to the location compared to that observed in Srivastava & Duraisamy (2021). The residual convergence plot when the T3A case is solved with the augmented model is shown in Fig. 5. The convergence characteristics are far superior compared to what was seen in Srivastava & Duraisamy (2021). This is because of the continuous nature of the functional form.

Testing The prediction results of this inferred augmentation on other flat plate cases are shown in Fig. 6. While

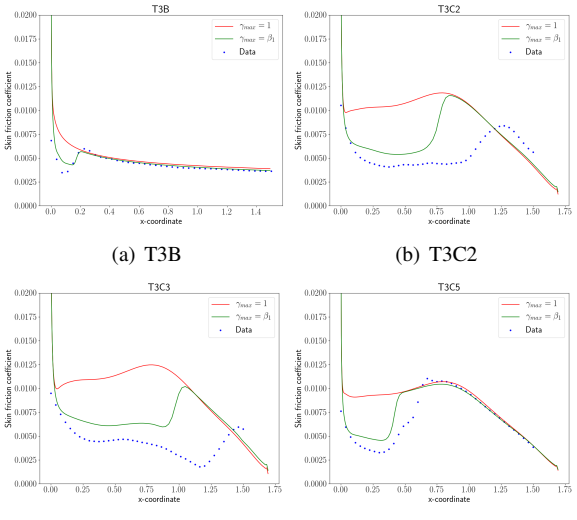

(a) T3B (b) T3C2

(c) T3C3 (d) T3C5

Figure 6. Skin friction predictions for T3 testing cases. Blue dots - Data; Red curves - Predictions using baseline model; Green curves - Predictions with parameters inferred for β_1 only

the transition predictions for T3B and T3C5 are reasonably accurate, transition is predicted significantly upstream of the true locations for T3C2 and T3C3. Even though the model was not trained on cases where transition occurs in adverse pressure gradients (which is the case for T3C2 and T3C3), these predictions are worse compared to those in Srivastava & Duraisamy (2021). This is because a continuous augmentation does not allow for sudden jumps in augmentation values within the feature space and hence intermittency has a more smeared growth. As soon as this smeared growth results in intermittency values high enough to facilitate k-production, transition is predicted. Hence, while C^0-continuous augmentation functions provide more laminarization and significantly better convergence characteristics, they also lead to a lower predictive accuracy for transition in adverse pressure gradient regions. This can be corrected in the future by using a more adaptive functional form for the augmentation function.

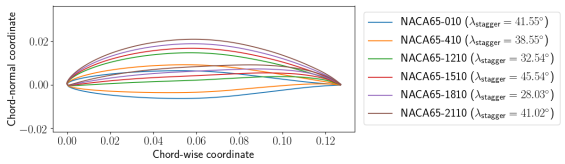

Figure 7. Blade geometries for compressor cascade

Figure 8. Mesh used for NACA 65-010 compressor cascade case

Inferring β_2

LES data for six compressor cascade cases was provided by RTRC. The geometries along with their blade stagger angles have been shown in Fig. 7. The mesh used for the NACA65-010 compressor cascade case is shown in Fig. 8. Similar meshes were used for other geometries. The inflow and outflow conditions for the compressor cascade cases have been shown in Tables 2 and 3. Fig. 9 shows the transition predictions made using the augmented model on a NACA 65-010 compressor cascade geometry. In this case, transition was predicted at the separation location which is significantly upstream of the actual transition location. Holding function parameters of β_1 constant at their inferred values, and assuming σ a constant baseline value of 1 for this step, function parameters for β_2 are inferred as follows.

Table 2. Inflow conditions common for all compressor cascade cases

$p_{0,\text{in}}$	$T_{0,\text{in}}$	Tu_{in}	$\nu_{t,\text{in}}/\nu_\infty$
14.7705724 PSI	288.5672892 K	1 %	10

Table 3. Outlet back-pressure and flow angles for compressor cascade cases

Cases	p_b (in PSI)	Flow angles
NACA65-010	14.695946	45°
NACA65-410	14.715946	45°
NACA65-1210	14.725946	45°
NACA65-1810	14.725946	45°
NACA65-1510	14.735946	60°
NACA65-2110	14.735946	60°

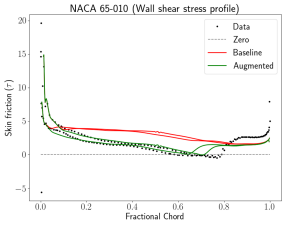

Figure 9. Wall shear stress predictions for NACA 65-010. Black dots - Data; Red curves - Predictions using baseline model; Green curves - Predictions with parameters inferred for β_1 only

Training The training process for β_2 was identical to that used for β_1 with three differences.

- Only the NACA 65-010 compressor cascade case was used to infer β_2.
- The feature-space for β_2 was divided into $30 \times 10 \times 10$ cells.
- The cost function $\mathscr{C}$ was set to the sum squared discrepancy between the predictions and LES data for wall shear stress.

Fig. 10 shows the wall shear stress profile predicted using the hierarchical augmentation. The predicted transition location shows excellent agreement with data. However, regions downstream of the transition location show a lower wall shear stress. This discrepancy is due to other inadequacies in the turbulence model and cannot be alleviated within the bounds set for the current augmentation.

Testing When tested on other compressor cascade configurations, the hierarchically augmented model showed a significant improvement compared to the results obtained

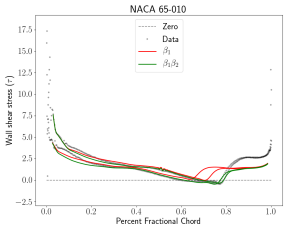

Figure 10. Wall shear stress predictions for NACA 65-010. Black dots - Data; Red curves - Predictions with parameters inferred for β_1 only; Green curves - Predictions with parameters inferred for both, β_1 and β_2

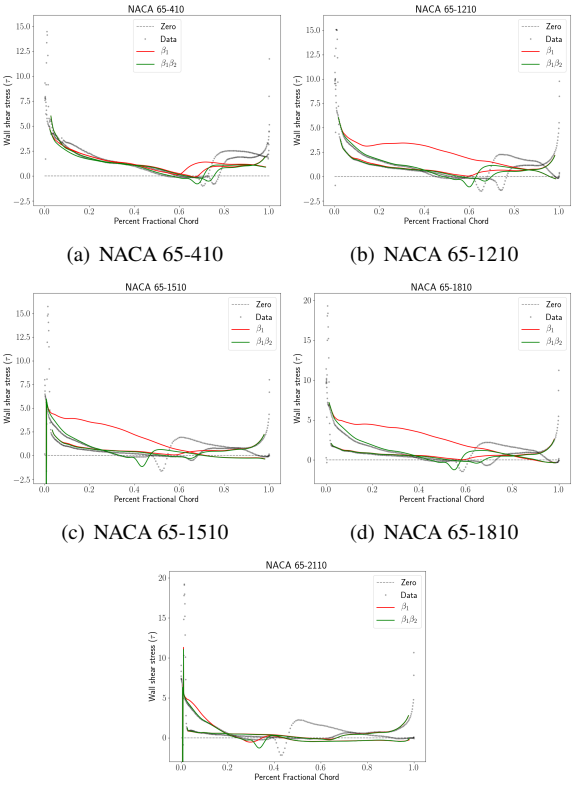

(a) NACA 65-410 (b) NACA 65-1210

(c) NACA 65-1510 (d) NACA 65-1810

(e) NACA 65-2110

Figure 11. Wall shear stress predictions for unseen compressor cascade cases. Black dots - Data; Red curves - Predictions with parameters inferred for β_1 only; Green curves - Predictions with parameters inferred for both, β_1 and β_2

using only β_1. The corresponding plots for NACA 65-410, NACA 65-1210, NACA 65-1510, NACA 65-1810 and NACA 65-2110 are shown in Fig. 11. In some cases transition is predicted considerably upstream of the true transition location. However, the model shows consistent and significant improvements in predictive accuracy even for these cases when compared to using just β_1.

Introducing σ

In the absence of any blending function to isolate effects of β_2, the predictive accuracy on the flat plate cases is abysmal when both β_1 and β_2 are used as shown by red curves in Fig. 12. However, when the blending function is used, the transition location predictions are restored (green curves) close to where they are predicted when using only β_1 (black dashed

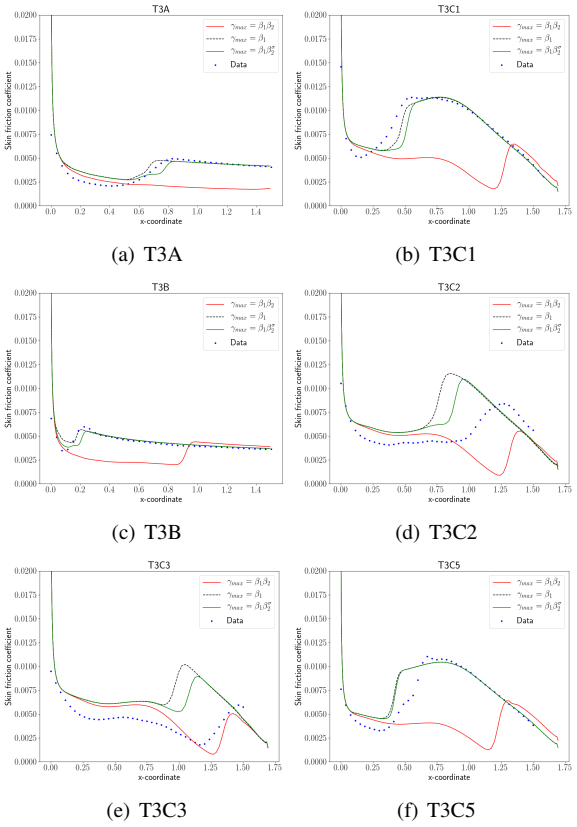

(a) T3A (b) T3C1

(c) T3B (d) T3C2

(e) T3C3 (f) T3C5

Figure 12. Skin friction predictions for T3 cases. Blue dots - Data; Black dashed curves - Predictions with parameters inferred for β_1 only; Red curves - Predictions with parameters inferred for both, β_1 and β_2, with $\sigma = 1$; Green curves - Predictions with parameters inferred for both, β_1 and β_2, with $\sigma = 1/(1+\exp(-(f_\sigma + 0.05)/0.003))$

curves). The predictions for transition under adverse pressure gradients (cases T3C2 and T3C3) actually improves when $\beta_1\beta_2^\sigma$ is used instead of just β_1. It should be noted here that the blending function has negligible effect on the compressor cascade cases.

CONCLUSIONS

This work describes a hierarchical augmentation technique to infer multiple augmentation functions that can address various model-form inadequacies manifested in different physical regimes. The process is demonstrated by consecutively inferring two augmentation functions within a bare-bones intermittency function that was added to Wilcox's 1988 k-ω model to predict transition caused by freestream disturbances and flow separation, respectively. An appropriate blending function is designed to isolate the effects of the second augmentation to cases involving separation-induced transition. The augmentation consistently improves predictions across a range of geometries and flow conditions. However, significant inaccuracies are observed for cases involving transition of attached flows in adverse pressure gradients and some cases involving separation-induced transition as well. In such cases, the augmentation predicts an early transition. Future work involves development of better features and a formal framework to optimize grid resolution in feature-space to reduce these inaccuracies. In addition to hierarchical augmentations, this work also provides a brief commentary on continuous functional forms for augmentations. As is demonstrated in the results, while such functional forms provide excellent solver convergence, they could slightly hamper accuracy for applications like bypass transition where sharp jumps in augmentation values in the feature-space might provide better results.

ACKNOWLEDGEMENTS

The authors acknowledge funding for this work from the ARPA-E Differentiate program (Award no. DE-AR0001201). The authors also thank RTRC for providing LES data for compressor cascade geometries.

REFERENCES

Durbin, Paul 2012 An intermittency model for bypass transition. *International Journal of Heat and Fluid Flow* **36**, 1–6.

Ge, Xuan, Arolla, Sunil & Durbin, Paul 2014 A bypass transition model based on the intermittency function. *Flow, turbulence and combustion* **93** (1), 37–61.

Holland, Jonathan R, Baeder, James D & Duraisamy, Karthik 2019 Towards integrated field inversion and machine learning with embedded neural networks for rans modeling. In *AIAA Scitech 2019 Forum*, p. 1884.

Parish, Eric J & Duraisamy, Karthik 2016 A paradigm for data-driven predictive modeling using field inversion and machine learning. *Journal of Computational Physics* **305**, 758–774.

Praisner, T. J. & Clark, J. P. 2004 Predicting Transition in Turbomachinery—Part I: A Review and New Model Development. *Journal of Turbomachinery* **129** (1), 1–13.

Schmelzer, Martin, Dwight, Richard P & Cinnella, Paola 2020 Discovery of algebraic reynolds-stress models using sparse symbolic regression. *Flow, Turbulence and Combustion* **104** (2), 579–603.

Sirignano, Justin, MacArt, Jonathan F & Freund, Jonathan B 2020 Dpm: A deep learning pde augmentation method with application to large-eddy simulation. *Journal of Computational Physics* **423**, 109811.

Srivastava, Vishal & Duraisamy, Karthik 2021 Generalizable physics-constrained modeling using learning and inference assisted by feature-space engineering. *Phys. Rev. Fluids* **6**, 124602.

Ströfer, Carlos A Michelén & Xiao, Heng 2021 End-to-end differentiable learning of turbulence models from indirect observations. *Theoretical and Applied Mechanics Letters* **11** (4), 100280.

Volpiani, Pedro Stefanin, Meyer, Morten, Franceschini, Lucas, Dandois, Julien, Renac, Florent, Martin, Emeric, Marquet, Olivier & Sipp, Denis 2021 Machine learning-augmented turbulence modeling for rans simulations of massively separated flows. *Physical Review Fluids* **6** (6), 064607.

Waschkowski, Fabian, Zhao, Yaomin, Sandberg, Richard & Klewicki, Joseph 2022 Multi-objective cfd-driven development of coupled turbulence closure models. *Journal of Computational Physics* **452**, 110922.

Wilcox, David C 1988 Reassessment of the scale-determining equation for advanced turbulence models. *AIAA journal* **26** (11), 1299–1310.